Iranian Journal of Fuzzy Systems

Volume 22, Number 6, (2025), pp. 21-39

Original paper

University of Sistan and Baluchestan

Triangular fuzzy solutions of coupled Boussinesq-Burgers Equations with uncertain parameters

R. Vana [1] and P. Karunakar [2]

[1,2] *Department of Mathematics, School of Advanced Sciences, VIT-AP University, Amaravati, India*

vvanarambabu@gmail.com, karunakarperumandla@gmail.com

Abstract

This article outlines the significance of the coupled Boussinesq-Burgers Equations (cBBEs) for the solution of fluid flow in complicated systems, with special emphasis on shallow water waves (SWW) close to the coasts and lakes. The manuscript also defines the Fuzzy Elzaki Adomian Decomposition Method (FEADM) as a new technique suitable for solving the cBBE's in crisp and fuzzy manners. Due to uncertainties in initial conditions caused by the fluid velocity or wave height, one parameter is taken to be a triangular fuzzy number (TFNs). Numerical implementations illustrate the performance of the FEADM against Homotopy Perturbation Method (HPM), Optimal Homotopy Asymptotic Method (OHAM) demonstrate that in terms of accuracy and efficiency, the method is superior. The proof of theorems also shows how the FEADM approaches the solution of nonlinear systems under uncertainties. These results of the research work show how useful the FEADM can be for the modeling of fluid dynamics in deterministic and fuzzy environments.

Keywords: Coupled Boussinesq-Burgers equations, FEADM, triangular fuzzy number, uncertainty modeling, convergence analysis, shallow water waves.

1 Introduction

The cBBEs is an important mathematical model used to understand fluid flow in dynamic systems, especially in relation to SWW. The water wave equations are a set of partial differential equations (PDEs) that describe water flow beneath a pressure surface, the motion of water bodies, and the flow in vertically well mixed water bodies. A notable feature of shallow water flow is that its horizontal scale is much larger than its vertical scale. Various generalized versions of the cBBEs have been solved in earlier studies [10, 21, 22].
The cBBEs have been studied for SWW near ocean beaches or in lakes [4, 29, 30],

$$\begin{aligned} \frac{\partial \mathcal{U}}{\partial \tau} + a\frac{\partial \mathcal{V}}{\partial \zeta} + b\mathcal{U}\frac{\partial \mathcal{U}}{\partial \zeta} = 0, \\ \frac{\partial \mathcal{V}}{\partial \tau} + c\frac{\partial^3 \mathcal{U}}{\partial \zeta^3} + d\frac{\partial}{\partial \zeta}(\mathcal{U}\mathcal{V}) = 0, \end{aligned} \tag{1}$$

subject to initial conditions,

$$\begin{aligned} \mathcal{U}(\zeta, 0) &= \frac{vq}{2} + \frac{vq}{2} tanh\left(\frac{-q\zeta - logw}{2}\right), \\ \mathcal{V}(\zeta, 0) &= \frac{-q^2}{8} sech^2\left(\frac{q\zeta + logw}{2}\right). \end{aligned} \tag{2}$$

Corresponding Author: P. Karunakar
Received: April 2025; Revised: September 2025; Accepted: October 2025.
https://doi.org/10.22111/ijfs.2025.51771.9143

The exact solutions of (1) subject to initial conditions (2) is [4, 29, 30],

$$\mathcal{U}(\zeta,\tau) = \frac{vq}{2} + \frac{vq}{2} tanh\left(\frac{vq^2\tau - q\zeta - logw}{2}\right),$$
$$\mathcal{V}(\zeta,\tau) = \frac{-q^2}{8} sech^2\left(\frac{q\zeta - vq^2\tau + logw}{2}\right).$$

Here, v, q and w are coefficients, $a, b, c,$ and d are nonzero real constants with ζ and τ representing space and time, respectively. The term $\mathcal{U}(\zeta,\tau)$ describes the horizontal fluid velocity, while $\mathcal{V}(\zeta,\tau)$ represents the height of the water surface above the horizontal bottom level.

With the progress in science and engineering, nonlinear evolution equations are now utilized to model physical phenomena in areas like fluid mechanics, plasma waves, solid-state physics, and chemical physics[6, 5]. In the past few decades, there has been a lot of focus on finding exact and numerical solutions to these problems. Many methods are available in the literature to solve these problems accurately and through analytical and numerical techniques. Mubaraki et al. [30] investigated exact analytical solutions for the cBBEs by applying the Kudryashov method and the exponential function expansion approach to obtain new solutions. Dong et al. [4] derived the non-local symmetry and Bäcklund transformation for the cBBEs using the truncated Painlevé and Riccati expansion methods, and investigate wave interactions with the consistent tanh expansion approach. The Residual Power Series Method (RPSM), which combines Taylor's series expansion is utilized to solve the cBBEs by authors [29]. The study examined water waves by applying bilinear-form and similarity-reduction methods in [12], and a hetero-Bäcklund transformation (BT) in [11] to the cBBEs. In [26], Lie group analysis was performed on a higher-order cBBEs. The cBBEs were also approached in [16] through the use of the Lie group. Li et al. [24] obtained rational solutions of the cBBEs system employing the Hirota bilinear method and the reduction process of Kadomtsev–Petviashvili's hierarchy. The controlled propagation of long-wave solutions for the cBBEs was addressed by [1]. Guo et al. [13] employed the homogeneous balance method and applied it to the solution of new multiple-soliton solutions of the higher-order cBBEs. Zhang and Chen [53] used the homogeneous balance method (HBM) in conjunction with asymptotic analysis to study the cBBEs. Wang [48] derived solutions of the cBBEs by using the truncated Painlevé analysis and the consistent tanh expansion method. Zuo and Zhang [53] used the HBM to prove that the coupled and higher-order Boussinesq-Burgers equations are completely integrable with multiple-soliton solutions. Rady et al. [34] obtained multi-soliton solutions and several rational wave solutions for the cBBEs by using the generalized tanh approach. In [33] periodic wave solutions for cBBEs were obtained through the use of Jacobi elliptic function method. The exact traveling wave solutions for the cBBEs were constructed by extending the method of homogeneous balance in [20]. The cBBEs in [36] were solved assuming Darboux transformations (DTs) exist for the spectral problem associated with cBBE. Liang et al. [25] presented some applications of the modified mapping method to the cBBEs to derive solutions. Li and Chen [23] appeared to have developed new parameters family of DTs for cBBEs, through some gauge Transformation based on spectral Problem from the lax pairs. In the study conducted by Podder et al. [35], a beta-derivative supported improved Bernoulli sub-equation function technique was developed to address the tfcBBEs. In their work, Zhang and Wang [51] managed to analyze the tfcBBEs by utilizing a Laplace adomian decomposition technique. Liu et al. [27] displayed various applications of their methodology on the tfcBBEs to deriv exact solutions using the modified extended tanh method, the improved $\left(\frac{G'}{G}\right)$, bifurcation, HPM and the fractional complex transform techniques are applied to solve ctfBBEs in [28]. Wang et al. [49] applied He's variational approach and the two-scale transform to derive periodic wave solutions for the ctfBBEs. Shi et al. [38] used the Lie symmetry analysis method to investigate the Lie point symmetry and similarity transformations of the ctfBBEs.

As many systems of PDEs do not have exact analytical solutions, several analytic and numerical techniques have been suggested to find approximate solutions to the cBBEs. In this regard, some studies have focused on finding numerical solutions to cBBEs, as seen in [4, 11, 12, 23, 33, 34].

In this study, the FEADM is used to find the analytical solution to the cBBEs in both crisp and fuzzy environments. The cBBEs are typically studied using precise values for the coefficients. However, in real-world scenarios, factors such as fluid velocity and wave height can introduce uncertainty into these coefficients. To address this, we model the initial conditions as TFNs instead of crisp values, accounting for this uncertainty. The main goal of this study is to enhance the cBBEs by incorporating uncertainty, providing a more accurate depiction of SSW dynamics. This article is significant because it applies the FEADM to manage uncertainty in the cBBEs. We showcase the effectiveness of this proposed technique by comparing its results with exact solutions. By closely examining these results together, we not only validate the effectiveness of this method but also deepen our understanding of wave phenomena in uncertain conditions. This method provides us with invaluable insights into wave interactions and propagation, helping us better comprehend the complexities of wave behavior across various scenarios.

2 Preliminaries

2.1 Triangular fuzzy numbers (TFNs):

The TFNs is defined as $\widetilde{v} = [v_l, v_m, v_u]$ with the membership function $\mu_{\widetilde{v}}$ is given by the following expression as [19, 39, 42],

$$\mu_{\widetilde{v}} = \begin{cases} \frac{\zeta - v_l}{v_m - v_l}, & \text{if } v_l \leq \zeta \leq v_m \\ \frac{v_u - \zeta}{v_u - v_m}, & \text{if } v_m \leq \zeta \leq v_u \\ 0, & \text{Otherwise} \end{cases}$$

2.2 Parametric form:

The parametric form represented by the ordered pair $\widetilde{v}$ may be used to define the TFNs using the r-cut technique. Specifically, $\widetilde{v} = [\underline{v}, \overline{v}]$, where $\widetilde{v} = [v_l + (v_m - v_l)\, r, v_u + (v_m - v_u)\, r]$, for $0 \leq r \leq 1$. Fuzzy numbers are often represented in a parametric form using the r-cut approach, where any interval denoted as $\widetilde{v} = [\underline{v}, \overline{v}]$ may be expressed in this parametric form as follows [18, 40, 41],

$$\widetilde{v} = [\underline{v}, \overline{v}] = \underline{v} + 2\gamma \Delta\widetilde{v}, \text{ where } \Delta\widetilde{v} = \frac{\overline{v} - \underline{v}}{2} = \frac{(v_u - v_l)(1 - r)}{2} \text{ and } 0 \leq \gamma \leq 1.$$

2.3 Elzaki transform:

The Elzaki Transform (ET) was invented by Tarig Elzaki and is based on the Fourier integral. In the time domain, NPDEs may be handled using this transform, [7, 8, 9],

$$Z = \left\{ u(\tau) : \exists\ \mathcal{M},\ \text{for } \varepsilon_1, \varepsilon_2 > 0 \ni\ |u(\tau)| < M e^{\frac{|\tau|}{\varepsilon_j}},\ \text{if } \tau \in (-1)^j \times [0, \infty) \right\}.$$

In the set Z, $\mathcal{M}$ must be a constant finite number, while $\varepsilon_1, \varepsilon_2$ may be either finite or infinite. The function $v(\tau)$ is defined by the value of $\mathbb{E}[v(\tau)] = \mathcal{V}(s)$.

$$\mathbb{E}[v(\tau)] = s \int_0^\infty v(\tau) e^{-\tau/s} d\tau = \mathcal{V}(s), \quad s \in (\varepsilon_1, \varepsilon_2).$$

3 Description of fuzzy Elzaki adomian decomposition method

The FEADM represents the Adomian Decomposition Method integrated with ET. The basic principles of EADM are given in [15, 44, 45, 46, 47]. A fuzzy model, which applies fuzzy sets for uncertainty, has almost exclusively found applications in system identification. These are rule-based systems that express relationships among variables with membership values, thereby handling vagueness and uncertainty. This research focuses on how FEADM enhances the accuracy of these models.

Consider a standard NPDEs with a source term as a fuzzy function $\widetilde{\vartheta}(\zeta, \tau; r, \gamma)$ as below

$$\mathbb{D}\widetilde{\mathcal{W}}(\zeta, \tau; r, \gamma) + \widetilde{v}\mathbb{R}\widetilde{\mathcal{W}}(\zeta, \tau; r, \gamma) + \mathbb{N}\widetilde{\mathcal{W}}(\zeta, \tau; r, \gamma) = \widetilde{\vartheta}(\zeta, \tau; r, \gamma), \tag{3}$$

with fuzzy initial condition

$$\widetilde{\mathcal{W}}(\zeta, \tau; r, \gamma) = \widetilde{\xi}(\zeta, 0; r, \gamma), \ \frac{\partial}{\partial \tau}\widetilde{\mathcal{W}}(\zeta, 0; r, \gamma) = \widetilde{\phi}(\zeta), \tag{4}$$

where the second order linear operator is defined as $\mathbb{D} = \frac{\partial^2}{\partial \tau^2}$. A linear operator of order less than $\mathbb{D}$ is represented by $\mathbb{R}$, while the nonlinear operator is denoted by $\mathbb{N}$.

The coefficient v in the equation (3) or initial conditions (4) is often uncertain because it depends on values measured in experiments. To address this, $\widetilde{v}$ can be expressed as intervals or fuzzy numbers, establishing bounds through a parametric approach. By representing $\widetilde{v}$ as a TFNs and utilizing the parametric form , equation (3) can be formulated. Applying the ET to equation (3) and utilizing the properties of the ET, after that using inverse ET, we get,

$$\begin{aligned} \mathbb{E}^{-1}\left(\mathbb{E}\left[\widetilde{\mathcal{W}}(\zeta, \tau; r, \gamma)\right]\right) =& \mathbb{E}^{-1}\left(s^2\ \mathbb{E}\left[\widetilde{\mathcal{W}}(\zeta, 0; r, \gamma)\right] + s^2\ \mathbb{E}\left[\widetilde{\vartheta}(\zeta, \tau; r, \gamma)\right]\right) \\ & - \mathbb{E}^{-1}\left(s^2\ \mathbb{E}\left[\widetilde{v}\mathbb{R}\widetilde{\mathcal{W}}(\zeta, \tau; r, \gamma) - \mathbb{N}\widetilde{\mathcal{W}}(\zeta, \tau; r, \gamma)\right]\right). \end{aligned} \tag{5}$$

On the right-hand side of equation (5), the first two terms are represented by $\widetilde{\mathcal{G}}(\zeta,\tau;r,\gamma)$.

$$\widetilde{\mathcal{W}}(\zeta,\tau;r,\gamma)=\widetilde{\mathcal{G}}(\zeta,\tau;r,\gamma)-\mathbb{E}^{-1}\left[s^2\ \mathbb{E}\left[(\underline{v}+2\gamma\Delta\widetilde{v})\,\mathbb{R}\widetilde{\mathcal{W}}(\zeta,\tau;r,\gamma)-\mathbb{N}\widetilde{\mathcal{W}}(\zeta,\tau;r,\gamma)\right]\right]. \tag{6}$$

Taking the solution as a series with $0\leq \mathbf{p}\leq 1$ embedding parameters, we obtain

$$\widetilde{\mathcal{W}}(\zeta,\tau;r,\gamma)=\sum_{k=0}^{\infty}\mathbf{p}^k\widetilde{\mathcal{W}}_k(\zeta,\tau;r,\gamma). \tag{7}$$

The nonlinear operator is expressed as follows,

$$\mathbb{N}\ \widetilde{\mathcal{W}}(\zeta,\tau;r,\gamma)=\sum_{k=0}^{\infty}\mathbf{p}^k\mathcal{A}_k. \tag{8}$$

The Adomian polynomials are expressed as $\mathcal{A}_k$, and the formula below is used to generate these polynomials [44, 45].

$$\mathcal{A}_k(\mathcal{A}_0,\mathcal{A},\mathcal{A}_2,\ldots,\mathcal{A}_n)=\frac{1}{n!}\left[\frac{\partial^n}{\partial p^n}\ \mathbb{N}\left(\sum_{k=0}^{\infty}\mathbf{p}^k\widetilde{\mathcal{W}}_k\right)\right]_{\mathbf{p}=0},k=0,1,2,3\ldots.$$

Equations (8) and (7) may be substituted into equation (6), we obtain

$$\begin{aligned}\sum_{k=0}^{\infty}\mathbf{p}^k\widetilde{\mathcal{W}}_k(\zeta,\tau;r,\gamma)=\widetilde{\mathcal{G}}(\zeta,\tau;r,\gamma)-\mathbf{p}\left(\mathbb{E}^{-1}\left[s^2\ \mathbb{E}\left[(\underline{v}+2\gamma\Delta\widetilde{v})\,\mathbb{R}\left(\sum_{k=0}^{\infty}\mathbf{p}^k\widetilde{\mathcal{W}}_k(\zeta,\tau;r,\gamma)\right)\right]\right]\right)\\ -\mathbf{p}\left(\mathbb{E}^{-1}\left[s^2\ \mathbb{E}\left[\sum_{k=0}^{\infty}\mathbf{p}^k\mathcal{A}_k\right]\right]\right).\end{aligned} \tag{9}$$

By comparing the coefficients of corresponding powers of '$\mathbf{p}$' on both sides of equation (9)

$$\begin{aligned}&\mathbf{p}^0:\widetilde{\mathcal{W}}_0(\zeta,\tau;r,\gamma)=\widetilde{\mathcal{G}}(\zeta,\tau;r,\gamma),\\ &\mathbf{p}^1:\widetilde{\mathcal{W}}_1(\zeta,\tau;r,\gamma)=-\mathbb{E}^{-1}\left[s^2\ \mathbb{E}\left[\mathbb{R}\left(\widetilde{\mathcal{W}}_0(\zeta,\tau;r,\gamma)\right)+(\mathcal{A}_0)\right]\right],\\ &\qquad\qquad\vdots\\ &\mathbf{p}^k:\widetilde{\mathcal{W}}_k(\zeta,\tau;r,\gamma)=-\mathbb{E}^{-1}\left[s^2\ \mathbb{E}\left[\mathbb{R}\left(\widetilde{\mathcal{W}}_{k-1}(\zeta,\tau;r,\gamma)\right)+(\mathcal{A}_{k-1})\right]\right].\end{aligned}$$

The solution of (3) is

$$\widetilde{\mathcal{W}}(\zeta,\tau;r,\gamma)=\lim_{p\to 1}\widetilde{\mathcal{W}}_k(\zeta,\tau;r,\gamma)=\widetilde{\mathcal{W}}_0(\zeta,\tau;r,\gamma)+\widetilde{\mathcal{W}}_1(\zeta,\tau;r,\gamma)+\ldots. \tag{10}$$

4 Implementation of EADM to the cBBEs

4.1 Implementation of EADM to the cBBEs in crisp environment

The goal of this section is to utilize the capabilities of the previously discussed EADM and focus on its application to cBBEs. By adopting this innovative approach, we can explore the behavior of this system of NPDEs in greater detail. We apply the ET on both sides of equation (1), we obtain

$$\begin{aligned}\mathbb{E}[\mathcal{U}(\zeta,\tau)]&=s^2\ \mathcal{U}(\zeta,0)-s\mathbb{E}\left[a\frac{\partial\mathcal{V}}{\partial\zeta}+b\mathcal{U}\frac{\partial\mathcal{U}}{\partial\zeta}\right],\\ \mathbb{E}[\mathcal{V}(\zeta,\tau)]&=s^2\ \mathcal{V}(\zeta,0)-s\mathbb{E}\left[c\frac{\partial^3\mathcal{U}}{\partial\zeta^3}+d\frac{\partial}{\partial\zeta}(\mathcal{U}\mathcal{V})\right].\end{aligned} \tag{11}$$

Inverse ET is applied on both sides of (11),

$$\begin{aligned}\mathcal{U}(\zeta,\tau)&=\mathbb{E}^{-1}\left[s^2\ \mathcal{U}(\zeta,0)\right]-\mathbb{E}^{-1}\left[s\mathbb{E}\left[a\frac{\partial\mathcal{V}}{\partial\zeta}+b\mathcal{U}\frac{\partial\mathcal{U}}{\partial\zeta}\right]\right],\\ \mathcal{V}(\zeta,\tau)&=\mathbb{E}^{-1}\left[s^2\ \mathcal{V}(\zeta,0)\right]-\mathbb{E}^{-1}\left[s\mathbb{E}\left[c\frac{\partial^3\mathcal{U}}{\partial\zeta^3}+d\frac{\partial}{\partial\zeta}(\mathcal{U}\mathcal{V})\right]\right].\end{aligned} \tag{12}$$

Using ADM to equation (12), we obtain,

$$\begin{aligned}\sum_{k=0}^{\infty}\mathbf{p}^k\mathcal{U}_k(\zeta,\tau)&=\mathcal{U}(\zeta,0)-\mathbf{p}\left(\mathbb{E}^{-1}\left[s\mathbb{E}\left[a\frac{\partial}{\partial\zeta}\sum_{k=0}^{\infty}\mathbf{p}^k\mathcal{V}_k(\zeta,\tau)+b\sum_{k=0}^{\infty}\mathbf{p}^k\mathcal{A}_{1k}(\mathcal{U})\right]\right]\right),\\ \sum_{k=0}^{\infty}\mathbf{p}^k\mathcal{V}_k(\zeta,\tau)&=\mathcal{V}(\zeta,0)-\mathbf{p}\left(\mathbb{E}^{-1}\left[s\mathbb{E}\left[c\frac{\partial^3}{\partial\zeta^3}\sum_{k=0}^{\infty}\mathbf{p}^k\mathcal{U}_k(\zeta,\tau)+d\sum_{k=0}^{\infty}\mathbf{p}^k\mathcal{A}_{2k}(\mathcal{UV})\right]\right]\right).\end{aligned}\tag{13}$$

For the nonlinear term $\mathcal{U}\frac{\partial\mathcal{U}}{\partial\zeta}$, first few Adomain polynomials are $\mathcal{A}_{1k}(\mathcal{U})$

$$\begin{aligned}\mathcal{A}_{10}(\mathcal{U})&=\mathcal{U}_0\frac{\partial\mathcal{U}_0}{\partial\zeta},\\ \mathcal{A}_{11}(\mathcal{U})&=\mathcal{U}_0\frac{\partial\mathcal{U}_1}{\partial\zeta}+\mathcal{U}_1\frac{\partial\mathcal{U}_0}{\partial\zeta},\\ &\vdots\end{aligned}$$

For the nonlinear term $\frac{\partial}{\partial\zeta}(\mathcal{UV})$, first few Adomain polynomials are $\mathcal{A}_{2k}(\mathcal{UV})$

$$\begin{aligned}\mathcal{A}_{20}(\mathcal{UV})&=\mathcal{U}_0\frac{\partial\mathcal{V}_0}{\partial\zeta}+\mathcal{V}_0\frac{\partial\mathcal{U}_0}{\partial\zeta},\\ \mathcal{A}_{21}(\mathcal{UV})&=\mathcal{U}_0\frac{\partial\mathcal{V}_1}{\partial\zeta}+\mathcal{U}_1\frac{\partial\mathcal{V}_0}{\partial\zeta}+\mathcal{V}_0\frac{\partial\mathcal{U}_1}{\partial\zeta}+\mathcal{V}_1\frac{\partial\mathcal{U}_0}{\partial\zeta},\\ &\vdots\end{aligned}$$

Comparing the coefficients of equivalent powers of '$\mathbf{p}$' on both sides of (13)

$$\begin{aligned}\mathbf{p}^0:\mathcal{U}_0(\zeta,\tau)&=\mathcal{U}(\zeta,0)=\frac{vq}{2}+\frac{vq}{2}tanh\left(\frac{-q\zeta-logw}{2}\right),\\ \mathcal{V}_0(\zeta,\tau)&=\mathcal{V}_0(\zeta,0)=\frac{-q^2}{8}sech^2\left(\frac{q\zeta+logw}{2}\right).\\ \mathbf{p}^1:\mathcal{U}_1(\zeta,\tau)&=t\left(\frac{q^3sinh(m)}{16cosh(m)^3}-\frac{v\,q^2\Big(\tanh(m)^2-1\Big)(vq-vqtanh(m))}{4}\right),\\ \mathcal{V}_1(\zeta,\tau)&=t\left(\frac{vq^4n^2}{16}+\frac{vq^4n}{16cosh(m)^2}+\frac{vq^4tanh(m)^2n}{8}-\frac{q^3\sinh(m)\left(\frac{vq}{2}-\frac{vqtanh(m)}{2}\right)}{4cosh(m)^3}\right),\\ &\vdots\end{aligned}$$

where $m=\frac{\log(w)}{2}+\frac{q\zeta}{2}, n=tanh(m)^2-1$.
The solution of (1) is

$$\begin{aligned}\mathcal{U}(\zeta,\tau)&=\mathcal{U}_0(\zeta,\tau)+\mathcal{U}_1(\zeta,\tau)+\mathcal{U}_2(\zeta,\tau)+\ldots,\\ \mathcal{V}(\zeta,\tau)&=\mathcal{V}_0(\zeta,\tau)+\mathcal{V}_1(\zeta,\tau)+\mathcal{V}_2(\zeta,\tau)+\ldots.\end{aligned}\tag{14}$$

4.2 Implementation of FEADM to the cBBEs in fuzzy environment

This section examines the fuzzy solution of coupled fuzzy BBEs, where the initial condition (2) is represented as a TFNs. The coefficient of this condition is affected by variables like fluid velocity and water surface height above the horizontal bottom level, which often lack precise or exact values. This method effectively captures the inherent uncertainty in these parameters. By representing the initial condition (2) as a TFNs,

$$\begin{aligned}\widetilde{\mathcal{U}}(\zeta,0;r,\gamma)&=\frac{(\underline{v}+2\gamma\Delta\widetilde{v})\,q}{2}+\frac{(\underline{v}+2\gamma\Delta\widetilde{v})\,q}{2}tanh\left(\frac{-q\zeta-logw}{2}\right),\\ \widetilde{\mathcal{V}}(\zeta,0;r,\gamma)&=\frac{-q^2}{8}sech^2\left(\frac{q\zeta+logw}{2}\right).\end{aligned}\tag{15}$$

A fuzzy version of the governing cBBES (1) can be developed as fuzzy form,

$$\begin{aligned} \frac{\partial \widetilde{\mathcal{U}}}{\partial \tau} + a\frac{\partial \widetilde{\mathcal{V}}}{\partial \zeta} + b\widetilde{\mathcal{U}}\frac{\partial \widetilde{\mathcal{U}}}{\partial \zeta} = 0, \\ \frac{\partial \widetilde{\mathcal{V}}}{\partial \tau} + c\frac{\partial^3 \widetilde{\mathcal{U}}}{\partial \zeta^3} + d\frac{\partial}{\partial \zeta}\left(\widetilde{\mathcal{U}}\widetilde{\mathcal{V}}\right) = 0. \end{aligned} \tag{16}$$

Here, dealing with the system of fuzzy nonlinear PDEs to solve the coupled fuzzy BBEs (16) presents a challenging task. Several research studies have explored different approaches to solving interval or fuzzy nonlinear PDEs utilizing a variety of semi-analytical and numerical methods. For additional information, readers are encouraged to consult the publications listed in [3, 18, 19, 35, 37, 39, 42, 40, 41, 43, 52]. The coupled fuzzy BBEs (16) can be effectively addressed through a convergent series approach.

In order to solve the coupled fuzzy BBEs (16) with the specified fuzzy initial condition (15), we use the FEADM approach with the help of TFNs. By utilizing a parameter-based technique, the FEADM enhances the fuzzy solutions and provides reliable estimates, even in situations where traditional methods may struggle.

By using FEADM, the fuzzy initial condition (15) may be used to solve the coupled fuzzy BBEs equation (16) as follows,

$$\begin{aligned} \sum_{k=0}^{\infty} \mathbf{p}^k \widetilde{\mathcal{U}}_k(\zeta,\tau;r,\gamma) =& \widetilde{\mathcal{U}}(\zeta,0;r,\gamma) - \mathbf{p}\left(\mathbb{E}^{-1}\left[s\mathbb{E}\left[a\frac{\partial}{\partial \zeta}\sum_{k=0}^{\infty}\mathbf{p}^k \widetilde{\mathcal{V}}_k(\zeta,\tau;r,\gamma)\right]\right]\right) \\ & - \mathbf{p}\left(\mathbb{E}^{-1}\left[s\mathbb{E}\left[b\sum_{k=0}^{\infty}\mathbf{p}^k \mathcal{A}_{1k}\left(\widetilde{\mathcal{U}}\right)\right]\right]\right), \\ \sum_{k=0}^{\infty} \mathbf{p}^k \widetilde{\mathcal{V}}_k(\zeta,\tau;r,\gamma) =& \widetilde{\mathcal{V}}(\zeta,0;r,\gamma) - \mathbf{p}\left(\mathbb{E}^{-1}\left[s\mathbb{E}\left[c\frac{\partial^3}{\partial \zeta^3}\sum_{k=0}^{\infty}\mathbf{p}^k \widetilde{\mathcal{U}}_k(\zeta,\tau;r,\gamma)\right]\right]\right) \\ & - \mathbf{p}\left(\mathbb{E}^{-1}\left[s\mathbb{E}\left[d\sum_{k=0}^{\infty}\mathbf{p}^k \mathcal{A}_{2k}\left(\widetilde{\mathcal{U}}\widetilde{\mathcal{V}}\right)\right]\right]\right). \end{aligned} \tag{17}$$

By comparing the coefficients of like powers of '$\mathbf{p}$' on both sides of equation (17), the following results are derived,

$$\begin{aligned} \mathbf{p}^0 :\ \widetilde{\mathcal{U}}_0(\zeta,\tau;r,\gamma) = \widetilde{\mathcal{U}}(\zeta,0;r,\gamma) &= \frac{(\underline{v}+2\gamma\Delta\widetilde{v})\,q}{2} + \frac{(\underline{v}+2\gamma\Delta\widetilde{v})\,q}{2} tanh\left(\frac{-q\zeta - logw}{2}\right) \\ &= \frac{q\left(\frac{r}{2}-\gamma(r-1)\right)}{2} - \frac{q\tanh\left(\frac{\log(w)}{2}+\frac{q\zeta}{2}\right)\left(\frac{r}{2}-\gamma\,(r-1)\right)}{2}, \\ \widetilde{\mathcal{V}}_0(\zeta,\tau;r,\gamma) = \widetilde{\mathcal{V}}(\zeta,0;r,\gamma) &= \frac{-q^2}{8} sech^2\left(\frac{q\zeta+logw}{2}\right) \\ &= -\frac{q^2}{8\ cosh\left(\frac{\log(w)}{2}+\frac{q\zeta}{2}\right)^2}, \end{aligned}$$

$$\begin{aligned} \mathbf{p}^1 :\ \widetilde{\mathcal{U}}_0(\zeta,\tau;r,\gamma) &= t\left(\frac{q^3 sinh(m)}{16 cosh(m)^3} - \frac{q^2 n\,(qK - qK tanh(m))\,K}{4}\right), \\ \widetilde{\mathcal{V}}_0(\zeta,\tau;r,\gamma) &= t\left(\frac{q^4 n^2 K}{16} + \frac{q^4 nK}{16 cosh\,(m)^2} + \frac{q^4 \tanh(m)^2 nK}{8}\right) \\ &= t\left(-\frac{q^3 sinh\,(m)\left(\frac{qK}{2} - \frac{qtanh(m)K}{2}\right)}{4 cosh\,(m)^3}\right), \\ &\text{where } m = \frac{\log(w)}{2} + \frac{q\zeta}{2}, n = \tanh(m)^2 - 1, K = \frac{r}{2} - \gamma(r-1). \end{aligned}$$

$$\vdots$$

The fuzzy series solution of (16) is

$$\begin{aligned}\mathcal{U}(\zeta,\tau;r,\gamma)&=\lim_{p\to 1}\widetilde{\mathcal{U}}_k(\zeta,\tau;r,\gamma)=\mathcal{U}_0(\zeta,\tau;r,\gamma)+\mathcal{U}_1(\zeta,\tau;r,\gamma)+\ldots,\\ \mathcal{V}(\zeta,\tau;r,\gamma)&=\lim_{p\to 1}\widetilde{\mathcal{V}}_k(\zeta,\tau;r,\gamma)=\mathcal{V}_0(\zeta,\tau;r,\gamma)+\mathcal{V}_1(\zeta,\tau;r,\gamma)+\ldots.\end{aligned}\tag{18}$$

4.3 Convergence analysis

We investigate the convergence of FEADM for nonlinear problems in this section, for a better understanding of the method. We present the sufficient conditions that are required for the convergence and associated error estimate. First of all, let us present the FEADM, which can be practically and efficiently used in solving problems involving nonlinear phenomena. It also helps in better convergence and estimating errors, as explained in [2, 17, 31]. The conditions that ensure convergence are derived in this paper. An error analysis is also presented to indicate the degree to which approximation results are credible and reveal facts on the drawbacks of the proposed technique. By carefully selecting the appropriate parameters and conditions, FEADM can be optimized to deliver reliable solutions for even the most complex nonlinear problems. The convergence analysis is given in the following theorems.

Theorem 4.1. *Let $\mathcal{U}$ and $\mathcal{V}$ be Banach spaces, and let $\mathcal{N}:\mathcal{U}\to\mathcal{V}$ be a contraction mapping such that for all $\widetilde{u},\widetilde{u}^*\in\mathcal{U}$,*

$$\|\mathcal{N}(\widetilde{u})-\mathcal{N}(\widetilde{u}^*)\|\leq\delta\|\widetilde{u}-\widetilde{u}^*\|,\ \delta\in(0,1).\tag{19}$$

Therefore, by Banach's fixed point theorem, $\mathcal{N}$ has a unique fixed point, denoted by $\widetilde{u}$, such that $\mathcal{N}(\widetilde{u})=\widetilde{u}$. The sequence generated by the FEADM is assumed to take the following form: $\widetilde{\mathcal{U}}_n=\mathcal{N}\left(\widetilde{\mathcal{U}}_{n-1}\right)$, $\widetilde{\mathcal{U}}_{n-1}=\sum_{k=0}^{n-1}\widetilde{u}_k, n=1,2,\ldots$ and let $\widetilde{\mathcal{U}}_0=\widetilde{u}_0\in\mathbb{B}_{\mathbf{r}}(\widetilde{u})$ where $\mathbb{B}_{\mathbf{r}}(\widetilde{u})=\{\widetilde{u}^*\in\widetilde{\mathcal{U}}\mid\|\widetilde{u}^*-\widetilde{u}\|<\mathbf{r}\}$, then we have

(i) $\|\widetilde{\mathcal{U}}_n-\widetilde{u}\|\leq\delta^n\|\widetilde{u}_0-\widetilde{u}\|$.

(ii) $\widetilde{\mathcal{U}}_n\in\mathbb{B}_{\mathbf{r}}(\widetilde{u})$.

(iii) $\lim_{n\to\infty}\widetilde{\mathcal{U}}_n=\widetilde{u}$.

Proof. The induction technique is used to prove part (i) of the given theorem. For n=1, $\|\widetilde{\mathcal{U}}_1-\widetilde{u}\|=\|\mathcal{N}\left(\widetilde{\mathcal{U}}_0\right)-\mathcal{N}(\widetilde{u})\|\leq\delta\|\widetilde{u}_0-\widetilde{u}\|$ (from equation (19)), let us suppose that $\|\widetilde{\mathcal{U}}_{n-1}-\widetilde{u}\|\leq\delta^{n-1}\|\widetilde{u}_0-\widetilde{u}\|$ as induction hypothesis then

$$\begin{aligned}\|\widetilde{\mathcal{U}}_n-\widetilde{u}\|&\leq\|\mathcal{N}\left(\widetilde{\mathcal{U}}_{n-1}\right)-\mathcal{N}(\widetilde{u})\|\\ &\leq\delta\|\widetilde{\mathcal{U}}_{n-1}-\widetilde{u}\|\\ &\leq\delta\delta^{n-1}\|\widetilde{u}_0-\widetilde{u}\|\ \text{(from induction hypothesis)}\\ &\leq\delta^n\|\widetilde{u}_0-\widetilde{u}\|.\end{aligned}$$

Hence, $\|\widetilde{\mathcal{U}}_n-\widetilde{u}\|\leq\delta^n\|\widetilde{u}_0-\widetilde{u}\|$. Utilizing (i), we have $\|\widetilde{\mathcal{U}}_n-\widetilde{u}\|\leq\delta^n\|\widetilde{u}_0-\widetilde{u}\|\leq\delta^n\mathbf{r}<\mathbf{r}$. This implies $\widetilde{\mathcal{U}}_n\in\mathbb{B}_{\mathbf{r}}(\widetilde{u})$. From (i), we have $\|\widetilde{\mathcal{U}}_n-\widetilde{u}\|\leq\delta^n\|\widetilde{u}_0-\widetilde{u}\|$. Since for δ in $(0,1)$, $\lim_{n\to\infty}\delta^n=0$, we have that $\lim_{n\to\infty}\|\widetilde{\mathcal{U}}_n-\widetilde{u}\|=0$. Hence, $\lim_{n\to\infty}\widetilde{\mathcal{U}}_n=\widetilde{u}$. □

Theorem 4.2. *Let the solution components $\widetilde{\mathcal{V}}_0,\widetilde{\mathcal{V}}_1,\widetilde{\mathcal{V}}_2,\ldots$ be defined as provided in equations (18). The series solution $\sum_{k=0}^{n-1}\widetilde{\mathcal{V}}_k(\zeta,\tau,r,\gamma)$ is convergent if $\exists\ \delta\in(0,1)$ such that $\|\widetilde{\mathcal{V}}_{k+1}\|\leq\delta\|\widetilde{\mathcal{V}}_k\|\forall k\geq k_0$ for some $k_0\in Z^+$.*

Proof. Define the sequence $\{\mathcal{S}_n\}_{n=0}^{\infty}$ as follows,

$$\begin{aligned}\mathcal{S}_0&=\widetilde{\mathcal{V}}_0,\\ \mathcal{S}_1&=\widetilde{\mathcal{V}}_0+\widetilde{\mathcal{V}}_1,\\ \mathcal{S}_2&=\widetilde{\mathcal{V}}_0+\widetilde{\mathcal{V}}_1+\widetilde{\mathcal{V}}_2,\\ &\vdots\\ \mathcal{S}_n&=\widetilde{\mathcal{V}}_0+\widetilde{\mathcal{V}}_1+\cdots+\widetilde{\mathcal{V}}_n,\end{aligned}$$

We need to demonstrate that $\{\mathcal{S}_n\}_{n=0}^{\infty}$ is a Cauchy sequence in the Hilbert space $\mathbb{R}$. Let,

$$\begin{aligned}\|\mathcal{S}_{n+1}-\mathcal{S}_n\| = \|\widetilde{\mathcal{V}}_{n+1}\| &\leq \delta\widetilde{\mathcal{V}}_n\\ &\leq \delta^2\widetilde{\mathcal{V}}_{n-1}\\ &\vdots\\ &\leq \delta^{n-k_0+1}\widetilde{\mathcal{V}}_{k_0}.\end{aligned}$$

For every $n, m \in Z^+, n \geq m > k_0$,.

$$\begin{aligned}\|\mathcal{S}_n-\mathcal{S}_m\| &= \|\left(\mathcal{S}_n-\mathcal{S}_{n-1}\right)+\left(\mathcal{S}_{n-1}-\mathcal{S}_{n-2}\right)+\cdots+\left(\mathcal{S}_{m+1}-\mathcal{S}_m\right)\|\\ &\leq \|\mathcal{S}_n-\mathcal{S}_{n-1}\|+\|\mathcal{S}_{n-1}-\mathcal{S}_{n-2}\|+\cdots+\|\mathcal{S}_{m+1}-\mathcal{S}_m\|\\ &\leq \delta^{n-k_0+1}\widetilde{\mathcal{V}}_{k_0}+\delta^{n-k_0+1}\widetilde{\mathcal{V}}_{k_0}+\cdots+\delta^{n-k_0+1}\widetilde{\mathcal{V}}_{k_0}\\ &= \left(\frac{1-\delta^{n-m}}{1-\delta}\right)\delta^{n-k_0+1}\widetilde{\mathcal{V}}_{k_0}.\end{aligned}$$

This implies, $\lim_{n,m\to\infty}\|\mathcal{S}_n-\mathcal{S}_m\|=0$. Therefore, $\{\mathcal{S}_n\}_{n=0}^{\infty}$ is a Cauchy sequence in the Hilbert space $\mathbb{R}$ and hence $\sum_{k=0}^{n-1}\widetilde{\mathcal{V}}_k\left(\zeta,\tau,r,\gamma\right)$ is convergent. □

5 Results and discussion

In order to analyze the behavior of the system under varying conditions, we employ the EADM to obtain approximate solutions for the cBBEs (1) in both crisp and fuzzy scenarios. The specified parameters of $a = 0.5$, $b = 2$, $c = 0.5$, and $d = 2$ are utilized in numerical simulations. These solutions allow for valuable insights into the system's dynamics.

5.1 Crisp case

This section presents the numerical solution of the cBBEs (1) to illustrate the effectiveness of the EADM at the specific values of $v = 0.5$, $q = -1$, and $w = 9$. A comparison is made between the results produced by our proposed method and those obtained through the HPM and the OHAM [14]. The results show that the EADM surpasses these alternative techniques, providing higher accuracy in the solutions. This shows that the EADM is strong and reliable for solving complex problems.

Table 1: Comparison of EADM and exact solutions of (1) at $\tau = 0.5$.

ζ	$\mathcal{U}$ (EADM)	$\mathcal{U}$ (Exact)	$\mathcal{V}$ (EADM)	$\mathcal{U}$ (Exact)
-1.0000	-0.0246	-0.0249	-0.0234	-0.0237
-0.8000	-0.0298	-0.0301	-0.0280	-0.0283
-0.6000	-0.0359	-0.0363	-0.0334	-0.0337
-0.4000	-0.0432	-0.0436	-0.0395	-0.0398
-0.2000	-0.0517	-0.0523	-0.0465	-0.0468
0.0000	-0.0618	-0.0624	-0.0543	-0.0546
0.2000	-0.0735	-0.0742	-0.0629	-0.0632
0.4000	-0.0870	-0.0877	-0.0722	-0.0723
0.6000	-0.1024	-0.1032	-0.0818	-0.0819
0.8000	-0.1198	-0.1205	-0.0915	-0.0915

Table 1 presents a comparative analysis between the outcomes derived from the EADM method and the exact solutions for two crucial variables: the horizontal velocity $\mathcal{U}(\zeta,\tau)$ and the water surface height $\mathcal{V}(\zeta,\tau)$ at $\tau = 0.5$, evaluated across different ζ values. The outcomes indicate a close approximation by the EADM method to the exact solutions, with minor variances observed. For instance, at $\zeta = -1.0000$, the computed horizontal velocity by EADM is -0.0246, whereas the exact solution stands at -0.0249, reflecting a marginal difference of 0.0003. Regarding the water surface height, the EADM computed value is -0.0234 compared to the exact value of -0.0237, with a similar distinction of 0.0003. As ζ increases, the disparities between the two methods remain minimal, reaffirming the precision

of the EADM method in approximating exact solutions across the entire ζ range. Notably, both $\mathcal{U}(\zeta,\tau)$ and $\mathcal{V}(\zeta,\tau)$ consistently exhibit negative values with increasing ζ, consistent with the expected system behavior. These results illustrate the reliability and accuracy of the EADM for solution approximation in this scenario, showcasing negligible deviations from the exact solutions.

Table 2: Comparison of exact and EADM results with absolute errors for $\mathcal{U}(\zeta,\tau)$ and $\mathcal{V}(\zeta,\tau)$ at $w=9$.

ζ	τ	$\mathcal{U}$ (Exact)	$\mathcal{U}$ (EADM)	$\mathcal{U}$ (Errors)	$\mathcal{V}$ (Exact)	$\mathcal{V}$ (EADM)	$\mathcal{V}$ (Errors)
0.1	0.1	-0.057167	-0.057123	4.3224×10^{-5}	-0.050631	-0.050608	2.2623×10^{-5}
0.1	0.2	-0.059747	-0.059592	1.5549×10^{-4}	-0.052608	-0.052528	7.9675×10^{-5}
0.1	0.3	-0.062428	-0.062118	3.1045×10^{-4}	-0.054634	-0.054479	1.5463×10^{-4}
0.1	0.4	-0.065211	-0.064730	4.8123×10^{-4}	-0.056706	-0.056476	2.3064×10^{-4}
0.1	0.5	-0.068100	-0.067459	6.4011×10^{-4}	-0.058824	-0.058534	2.9070×10^{-4}
0.2	0.1	-0.062428	-0.062383	4.5439×10^{-5}	-0.054634	-0.054612	2.1589×10^{-5}
0.2	0.2	-0.065211	-0.065048	1.6327×10^{-4}	-0.056706	-0.056631	7.5600×10^{-5}
0.2	0.3	-0.068100	-0.067774	3.2549×10^{-4}	-0.058824	-0.058679	1.4559×10^{-4}
0.2	0.4	-0.071095	-0.070591	5.0355×10^{-4}	-0.060986	-0.060771	2.1480×10^{-4}
0.2	0.5	-0.074199	-0.073531	6.6803×10^{-4}	-0.063188	-0.062921	2.6646×10^{-4}
0.3	0.1	-0.068100	-0.068052	4.7526×10^{-5}	-0.058824	-0.058804	2.0054×10^{-5}
0.3	0.2	-0.071095	-0.070924	1.7055×10^{-4}	-0.060986	-0.060916	6.9698×10^{-5}
0.3	0.3	-0.074199	-0.073859	3.3944×10^{-4}	-0.063188	-0.063055	1.3284×10^{-4}
0.3	0.4	-0.077414	-0.076890	5.2399×10^{-4}	-0.065428	-0.065235	1.9310×10^{-4}
0.3	0.5	-0.080742	-0.080049	6.9313×10^{-4}	-0.067704	-0.067469	2.3423×10^{-4}
0.4	0.1	-0.074199	-0.074149	4.9431×10^{-5}	-0.063188	-0.063170	1.7961×10^{-5}
0.4	0.2	-0.077414	-0.077237	1.7714×10^{-4}	-0.065428	-0.065366	6.1772×10^{-5}
0.4	0.3	-0.080742	-0.080390	3.5192×10^{-4}	-0.067704	-0.067588	1.1600×10^{-4}
0.4	0.4	-0.084185	-0.083643	5.4195×10^{-4}	-0.070011	-0.069846	1.6500×10^{-4}
0.4	0.5	-0.087744	-0.087029	7.1459×10^{-4}	-0.072346	-0.072152	1.9338×10^{-4}
0.5	0.1	-0.080742	-0.080691	5.1098×10^{-5}	-0.067704	-0.067688	1.5262×10^{-5}
0.5	0.2	-0.084185	-0.084002	1.8283×10^{-4}	-0.070011	-0.069959	5.1653×10^{-5}
0.5	0.3	-0.087744	-0.087381	3.6250×10^{-4}	-0.072346	-0.072251	9.4775×10^{-5}
0.5	0.4	-0.091420	-0.090863	5.5677×10^{-4}	-0.074705	-0.074575	1.3007×10^{-4}
0.5	0.5	-0.095215	-0.094483	7.3151×10^{-4}	-0.077083	-0.076939	1.4346×10^{-4}

Table 2 displays the outcomes obtained from varying ζ and τ with $w=9$ using the EADM, which includes the absolute errors between the exact solutions and the EADM-produced outcomes for $\mathcal{U}$ and $\mathcal{V}$. The table suggests that the EADM approach is an accurate method for approximating the exact solutions, as evidenced by the negligible absolute errors recorded. For example, when $\zeta=0.1$ and $\tau=0.1$, the precise value of $\mathcal{U}$ is -0.057167, while the EADM result is -0.057123, which yields an error of around 4.32×10^{-5}. Correspondingly, for $\mathcal{V}$, the accurate output is -0.050631, and the EADM output is -0.050608, which produces a minor error of 2.26×10^{-5}. As both ζ and τ increase, the absolute errors remain small but display a slight upward trend. Throughout all the cases in the table, the errors for both $\mathcal{U}$ and $\mathcal{V}$ consistently fall within the range of 10^{-5} to 10^{-4}. This confirms the EADM method's effectiveness and accuracy in approximating exact solutions.

Table 3 presents a comparison of absolute errors for two variables, $\mathcal{U}$ and $\mathcal{V}$, calculated using the EADM, HPM, and OHAM methods [14] across different ζ and τ values, with w fixed at 2. The errors for $\mathcal{U}$ and $\mathcal{V}$ are clearly reported for each method, highlighting the differences in their accuracy. The EADM errors, displayed in the first two columns, reveal that this method generally achieves smaller errors, especially at lower values of ζ and τ. For instance, at $\zeta=0.1$ and $\tau=0.1$, the absolute errors for $\mathcal{U}_{\text{EADM}}$ and $\mathcal{V}_{\text{EADM}}$ are 3.6245×10^{-5} and 4.9599×10^{-5}, respectively, both of which are lower than those obtained using the HPM and OHAM methods. As ζ and τ increase, the absolute errors show a slight increase, but the EADM method continues to deliver reliable results. For example, at $\zeta=0.5$ and $\tau=0.5$, the absolute errors for $\mathcal{U}_{\text{EADM}}$ and $\mathcal{V}_{\text{EADM}}$ rise to 5.5607×10^{-5} and 9.5194×10^{-4}, respectively. This increase in error reflects a slight degradation in accuracy while still demonstrating a clear advantage over the other methods. This highlights the efficiency of the EADM method in providing reliable approximations. The comparison between the methods indicates that while the EADM provides the most accurate results, the HPM and OHAM [14] also yield results with reasonable accuracy, although their errors tend to be higher, especially as ζ and τ increase. Additionally, the OHAM shows relatively smaller errors for $\mathcal{V}$ in some cases, particularly for larger values of ζ and τ, suggesting that it may be more effective in certain conditions.

Fig. 1 compares the solutions for the horizontal fluid velocity, $\mathcal{U}(\zeta,\tau)$, obtained through the EADM and the exact solution. It is plotted for specific parameter values: $\nu=0.5, q=-1$, and $w=9$. The spatial variable ζ is shown on the horizontal axis, while τ, representing time, is on the vertical axis. The panels display the approximate solutions at the second, third, and fourth terms of the EADM alongside the exact solution. The plots reveal a smooth transition in the velocity profile, with increasing accuracy as higher-order terms are included in the approximation. The bottom-right panel, depicting the exact solution, serves as a reference to evaluate the accuracy of the EADM. The close agreement

Table 3: Comparison of Absolute Errors for $\mathcal{U}$ and $\mathcal{V}$ at Various Values of ζ and τ and $w = 2$.

Absolute Errors for $\mathcal{U}$ and $\mathcal{V}$				Comparison of Errors for $\mathcal{U}_{\text{HPM}}$, $\mathcal{V}_{\text{HPM}}$, $\mathcal{U}_{\text{OHAM}}$, and $\mathcal{V}_{\text{OHPM}}$			
ζ	τ	$\mathcal{U}_{\text{EADM}}$	$\mathcal{V}_{\text{EADM}}$	$\mathcal{U}_{\text{HPM}}$ [14]	$\mathcal{V}_{\text{HPM}}$[14]	$\mathcal{U}_{\text{OHAM}}$[14]	$\mathcal{V}_{\text{OHAM}}$[14]
0.1	0.1	3.6245×10^{-5}	4.9599×10^{-5}	4.03765×10^{-5}	5.49815×10^{-5}	5.43565×10^{-5}	5.30293×10^{-5}
0.1	0.2	1.2466×10^{-4}	1.8142×10^{-4}	1.57743×10^{-4}	2.24577×10^{-4}	3.17229×10^{-5}	8.55529×10^{-6}
0.1	0.3	2.3451×10^{-4}	3.6926×10^{-4}	3.46200×10^{-4}	5.15476×10^{-4}	6.20012×10^{-5}	1.91443×10^{-4}
0.1	0.4	3.3520×10^{-4}	5.8521×10^{-4}	5.99524×10^{-4}	9.33935×10^{-4}	2.20592×10^{-4}	5.01892×10^{-4}
0.1	0.5	3.9727×10^{-4}	7.9874×10^{-4}	9.11191×10^{-4}	1.48572×10^{-3}	4.37526×10^{-4}	9.45668×10^{-4}
0.2	0.1	3.0976×10^{-5}	5.5661×10^{-5}	3.45343×10^{-5}	6.17326×10^{-5}	6.27431×10^{-5}	3.12906×10^{-5}
0.2	0.2	1.0545×10^{-4}	2.0235×10^{-4}	1.33936×10^{-4}	2.51026×10^{-4}	6.06192×10^{-5}	6.49797×10^{-5}
0.2	0.3	1.9557×10^{-4}	4.0875×10^{-4}	2.91679×10^{-4}	5.73647×10^{-4}	1.52649×10^{-7}	2.94577×10^{-4}
0.2	0.4	2.7377×10^{-4}	6.4177×10^{-4}	5.00967×10^{-4}	1.03482×10^{-3}	1.11857×10^{-4}	6.62723×10^{-4}
0.2	0.5	3.1393×10^{-4}	8.6578×10^{-4}	7.54752×10^{-4}	1.63915×10^{-3}	2.68365×10^{-5}	1.17404×10^{-3}
0.3	0.1	2.5140×10^{-5}	6.0908×10^{-5}	2.80601×10^{-5}	6.75811×10^{-5}	7.13609×10^{-5}	8.76219×10^{-6}
0.3	0.2	8.4293×10^{-5}	2.2021×10^{-4}	1.07664×10^{-4}	2.73710×10^{-4}	9.11785×10^{-5}	1.21023×10^{-4}
0.3	0.3	1.5298×10^{-4}	4.4178×10^{-4}	2.31765×10^{-4}	6.23007×10^{-4}	6.64983×10^{-5}	3.93977×10^{-4}
0.3	0.4	2.0719×10^{-4}	6.8774×10^{-4}	3.93103×10^{-4}	1.11945×10^{-3}	4.58083×10^{-6}	8.14078×10^{-4}
0.3	0.5	2.2461×10^{-4}	9.1779×10^{-4}	5.84236×10^{-4}	1.76633×10^{-3}	8.71313×10^{-5}	1.38462×10^{-3}
0.4	0.1	1.8829×10^{-5}	6.5136×10^{-5}	2.10557×10^{-5}	7.23025×10^{-5}	8.00687×10^{-5}	1.40750×10^{-5}
0.4	0.2	6.1534×10^{-5}	2.3430×10^{-4}	7.93485×10^{-5}	2.91751×10^{-4}	1.22900×10^{-5}	1.75296×10^{-4}
0.4	0.3	1.0747×10^{-4}	4.6707×10^{-4}	1.67436×10^{-4}	6.61637×10^{-4}	1.35937×10^{-4}	4.86954×10^{-4}
0.4	0.4	1.3663×10^{-4}	7.2130×10^{-4}	2.77729×10^{-4}	1.18453×10^{-3}	1.26768×10^{-4}	9.51621×10^{-4}
0.4	0.5	1.3094×10^{-4}	9.5270×10^{-4}	4.02528×10^{-4}	1.86226×10^{-3}	1.03094×10^{-4}	1.57112×10^{-3}
0.5	0.1	1.2153×10^{-5}	6.8178×10^{-5}	1.36435×10^{-5}	7.57082×10^{-5}	8.87114×10^{-5}	3.67202×10^{-5}
0.5	0.2	3.7578×10^{-5}	2.4405×10^{-4}	4.94924×10^{-5}	3.04426×10^{-4}	1.55217×10^{-4}	2.26450×10^{-4}
0.5	0.3	5.9859×10^{-5}	4.8359×10^{-4}	9.98476×10^{-5}	6.87978×10^{-4}	2.07217×10^{-4}	5.71013×10^{-4}
0.5	0.4	6.3394×10^{-5}	7.4108×10^{-4}	1.56977×10^{-4}	1.03084×10^{-3}	1.87026×10^{-4}	1.10746×10^{-3}
0.5	0.5	5.5607×10^{-5}	9.5194×10^{-4}	2.11301×10^{-4}	1.76465×10^{-3}	2.28055×10^{-4}	1.65496×10^{-3}

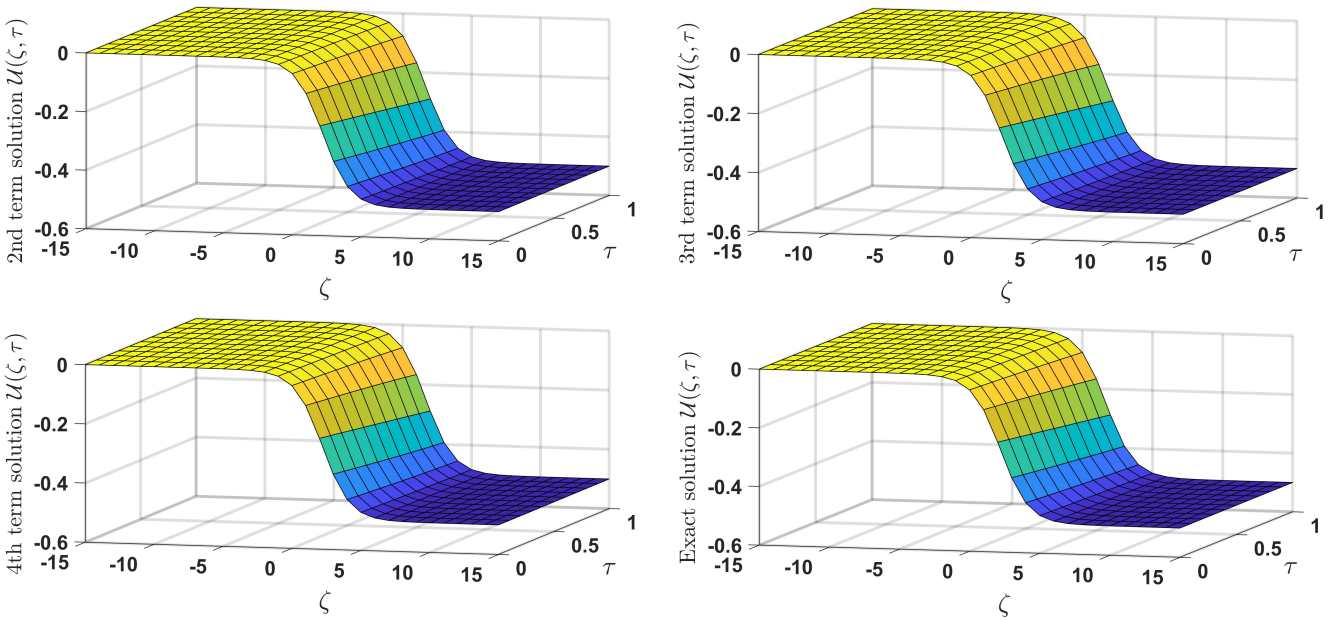

Figure 1: Comparison of EADM and exact solutions $\mathcal{U}(\zeta,\tau)$ at $v = 0.5, q = -1$ and $w = 9$.

between the EADM solutions and the exact solution highlights the method's effectiveness in modeling the behavior of the horizontal fluid velocity.

Fig. 2 illustrates the height of the water surface, $\mathcal{V}(\zeta,\tau)$, measured above a horizontal bottom level. The figure presents a comparison of the approximations of $\mathcal{V}(\zeta,\tau)$ obtained using the EADM method against the exact solution. This comparison is depicted across four panels: the top-left panel shows the second-term approximation, the top-right panel displays the third-term approximation, and the bottom-left panel features the fourth-term approximation, with the exact solution presented in the bottom-right panel. These visualizations clearly demonstrate how the EADM approximations converge towards the exact solution as more terms are included, illustrating the method's effectiveness in

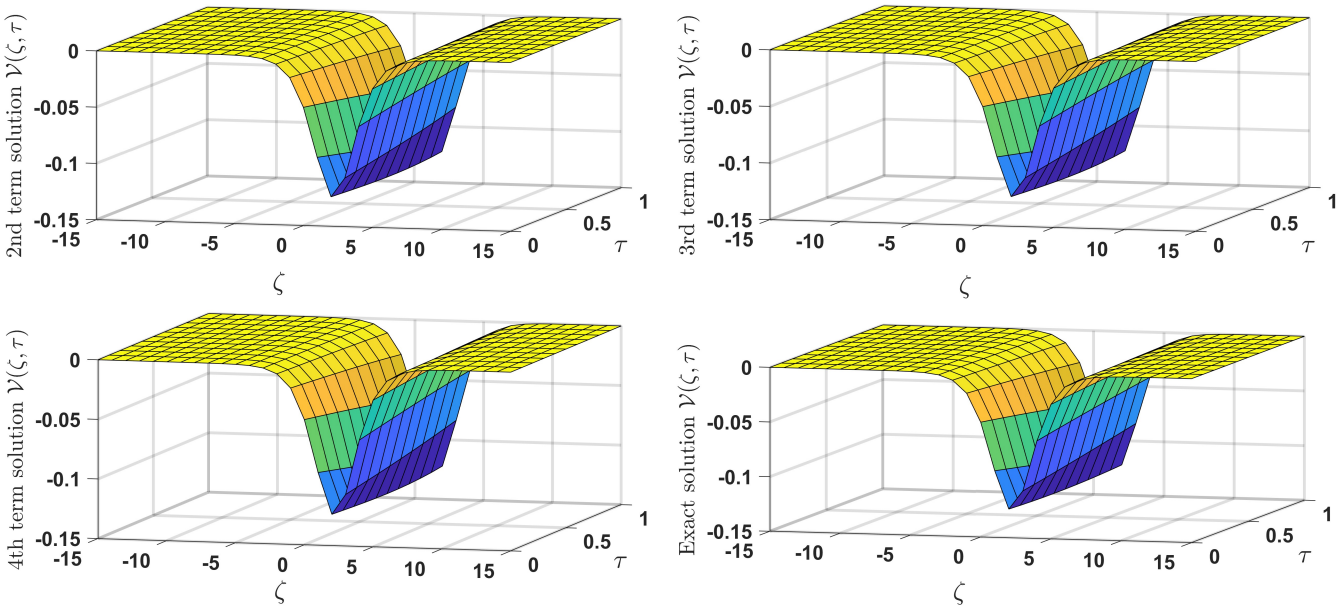

Figure 2: Comparison of EADM and exact solutions $\mathcal{V}(\zeta,\tau)$ at $v=0.5, q=-1$ and $w=9$.

accurately capturing the water surface profile. By incorporating the parameters $\nu=0.5$, $q=-1$, and $w=9$, the visual representations provide a comprehensive understanding of the behavior of $\mathcal{V}(\zeta,\tau)$ with respect to both the spatial and temporal variables ζ and τ. These plots effectively demonstrate the accuracy and reliability of the EADM.

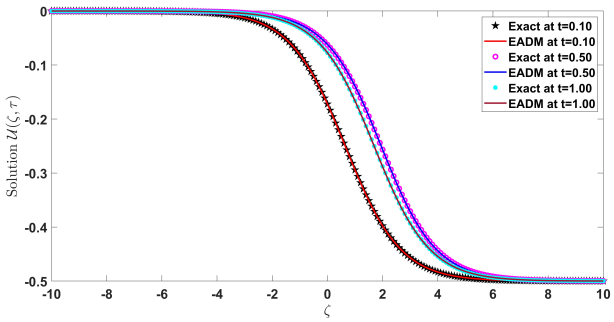

Figure 3: Comparison of EADM and exact solutions $\mathcal{U}(\zeta,\tau)$ at different values of τ.

The comparison of the horizontal fluid velocity, $\mathcal{U}(\zeta,\tau)$, determined by the EADM and the exact solutions at different time values is shown in Fig. 3. The spatial variable ζ is plotted with comparisons made at $\tau=0.10$, $\tau=0.50$, and $\tau=1.00$. The figure indicates a strong alignment between the EADM approximations and the exact solutions at all time points, highlighting the method's precision in modeling horizontal fluid velocity. This close correspondence demonstrates the effectiveness of EADM in accurately approximating $\mathcal{U}(\zeta,\tau)$ across both ζ and τ.

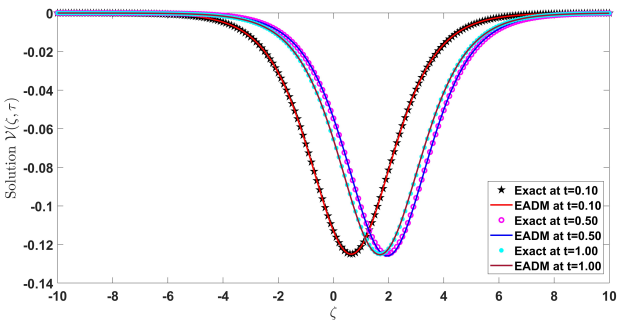

Figure 4: Comparison of EADM and exact solutions $\mathcal{V}(\zeta,\tau)$ at different values of τ.

Fig. 4, displays the exact solutions alongside the EADM solutions for the water surface height, $\mathcal{V}(\zeta,\tau)$, at various time levels τ. The horizontal axis represents the spatial variable ζ, while the vertical axis represents $\mathcal{V}(\zeta,\tau)$, which denotes the height of the water surface above a horizontal bottom level. The plot includes three time instances: $\tau = 0.10, \tau = 0.50$, and $\tau = 1.00$. For each time level, the EADM solutions (solid lines) closely align with the exact solutions (at various time levels), indicating the high accuracy of the EADM. The symmetric behavior of $\mathcal{V}(\zeta,\tau)$ around $\zeta = 0$ suggests a wave-like propagation pattern that evolves smoothly over time.

5.2 Fuzzy case

This section demonstrates the fuzzy solutions of the coupled fuzzy BBEs (16) to evaluate the effectiveness of the FEADM at $q = -1$ and $w = 9$. The initial condition (2) is expressed as a TFNs, $\widetilde{v} = [0, 0.5, 1]$, which effectively accounts for the uncertainty inherent in these parameters.

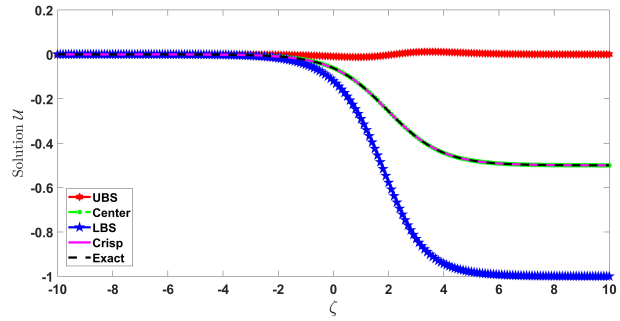

Figure 5: Comparison of crisp, fuzzy and exact solutions $\mathcal{U}$ at $q = -1, w = 9$ and $\tau = 0.5$.

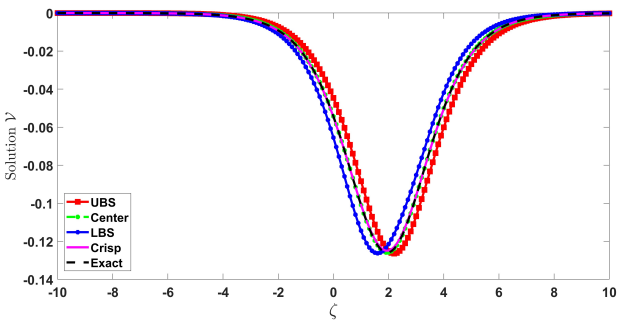

Figure 6: Comparison of crisp, fuzzy and exact solutions $\mathcal{V}$ at $q = -1, w = 9$ and $\tau = 0.5$.

Fig. 5 illustrates the comparison between crisp, fuzzy, and exact solutions of $\mathcal{V}$ for $q = -1, w = 9$, and $\tau = 0.5$. The

spatial variable ζ is plotted on the horizontal axis, and the solution $\mathcal{V}$ is plotted on the vertical axis. The fuzzy solution is represented as follows: the Upper Bound Solution (UBS) is shown in red, the Lower Bound Solution (LBS) is shown in blue, and the center solution is shown in green. These bounds account for the uncertainty in the fuzzy parameters. The crisp solution (magenta) and exact solution (black dashed line) are also shown for comparison. The results show that the bounds of the fuzzy solution closely include the exact solution, with the central solution aligning closely with both the exact and crisp solutions. The fuzzy solutions are useful in showing a range of possible results. The UBS is the maximum value, the LBS is the minimum value, and the center solution is the most likely value. The exact solution is closed to the center solution, which shows that the fuzzy approach gives a good approximation of the exact result.
In Fig. 6, displays compares crisp, fuzzy, and exact solutions $\mathcal{V}$ for specific parameter values $q = -1, w = 9$, and $\tau = 0.5$. The horizontal axis ζ represents the independent variable, while the vertical axis depicts the solution values. The plot includes five curves: the UBS in red, the central fuzzy solution (Center) in green, the LBS in blue, the crisp solution in solid blue, and the exact solution represented by the magenta dashed line. The fuzzy solutions (UBS, Center, and LBS) closely follow the exact solution, capturing uncertainty by showing slight variations around it. The crisp solution aligns well with the exact solution in some regions but diverges slightly due to its deterministic nature, lacking the flexibility to address fuzziness.

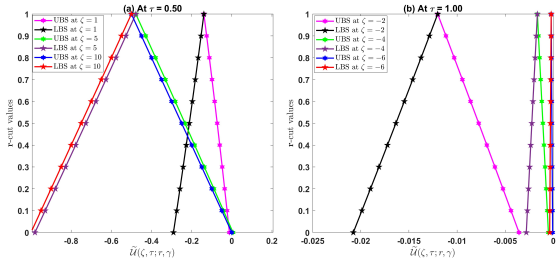

Figure 7: TFNs plots for $\widetilde{\mathcal{U}}$ at $q = -1, w = 9$ and $\tau = 0.5$.

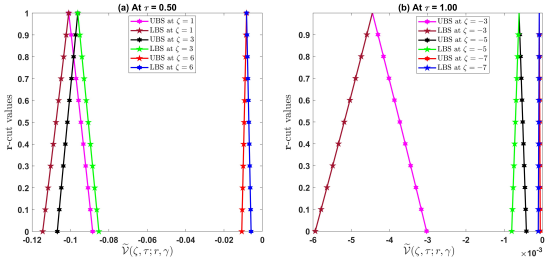

Figure 8: TFNs plots for $\widetilde{\mathcal{U}}$ at $q = -1, w = 9$ and $\tau = 0.5$.

Fig. 7, shows two plots, (a) and (b), which represent TFN plots for $\widetilde{\mathcal{U}}(\zeta, \tau; r, \gamma)$ at $q = -1, w = 9$, and different values of τ. In the left graph (a), for $\tau = 0.50$, TFNs are shown for $\zeta = 1, 5, 10$, while in the right graph (b), for $\tau = 1.00$, TFNs are plotted for $\zeta = -2, -4, -6$. The UBS are marked with magenta, blue, and red lines, and the LBS are represented by black, green, and purple lines. The shape of these solutions forms a triangle, where the top point of each triangle shows the most likely value. A key observation is that the triangles become narrower over time, meaning the length of the width between the lower bound and upper bound solutions decreases. This indicates that as τ increases, the solutions become more precise. Another important point is that the triangles shift towards the left for different values of ζ, showing changes in the fuzzy solution space. Comparing the two graphs, the reduction in width is more noticeable in (b) at $\tau = 1.00$, which further confirms that the length of width between the LBS and UBS reduces as time progresses.
Fig. 8 consists of two subplots, (a) and (b), which shows TFN plots for $\widetilde{\mathcal{V}}(\zeta, \tau; r, \gamma)$ at $q = -1, w = 9$, and different values of τ. The left subplot (a) represents $\tau = 0.50$ with TFNs for $\zeta = 1, 3, 6$, while the right subplot (b) corresponds to $\tau = 1.00$ with TFNs for $\zeta = -3, -5, -7$. In both graphs, UBS are shown using magenta, black, and red lines, while the LBS are represented by brown, green, and blue lines. The triangular shape of these solutions represents the fuzzy membership function, with the peak indicating the most likely value. An important observation is that the width between the LBS and UBS decreases as τ increases from 0.50 to 1.00. This implies that the range of possible

solutions becomes narrower and more precise over time. Additionally, the triangular shapes shift towards the left for different values of ζ, reflecting variations in the fuzzy solution space. Comparing the two subplots, it is evident that the reduction in width is more significant in (b) at $\tau = 1.00$. This confirms that the length of the width between the LBS and UBS decreases as time progresses, indicating that the solutions become more stable and well-defined.

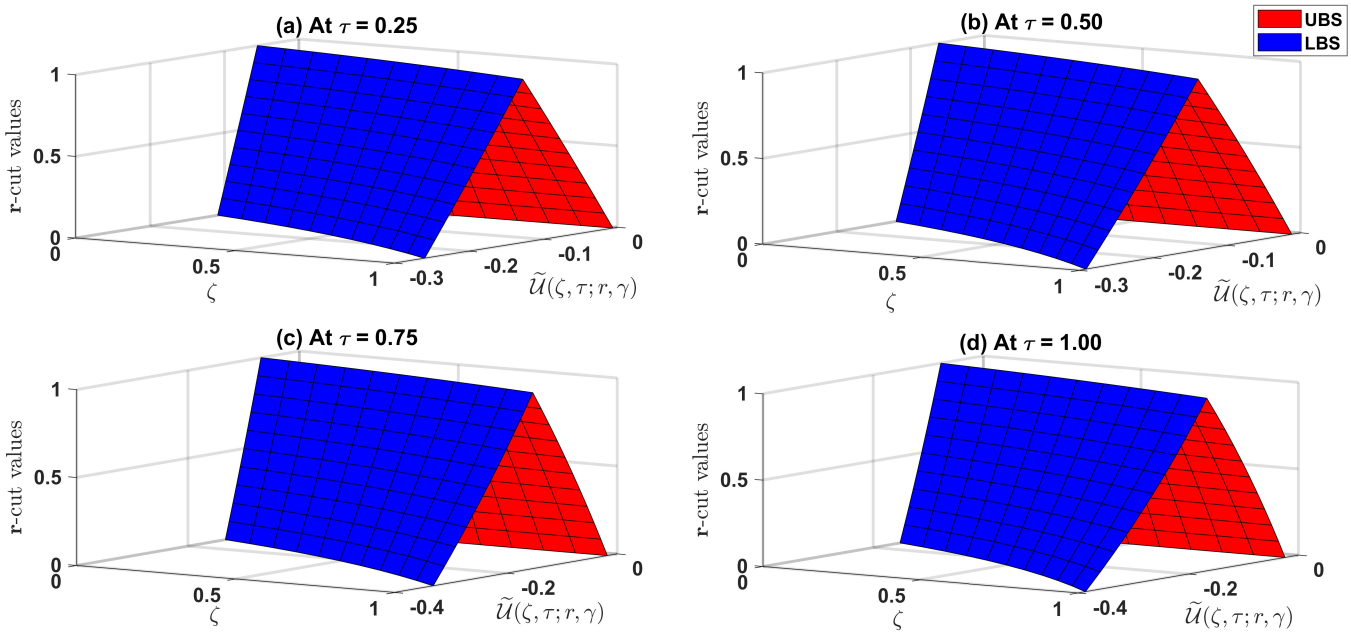

Figure 9: TFNs plots for $\widetilde{\mathcal{U}}$ at $q = -1, w = 9$ and different values of τ.

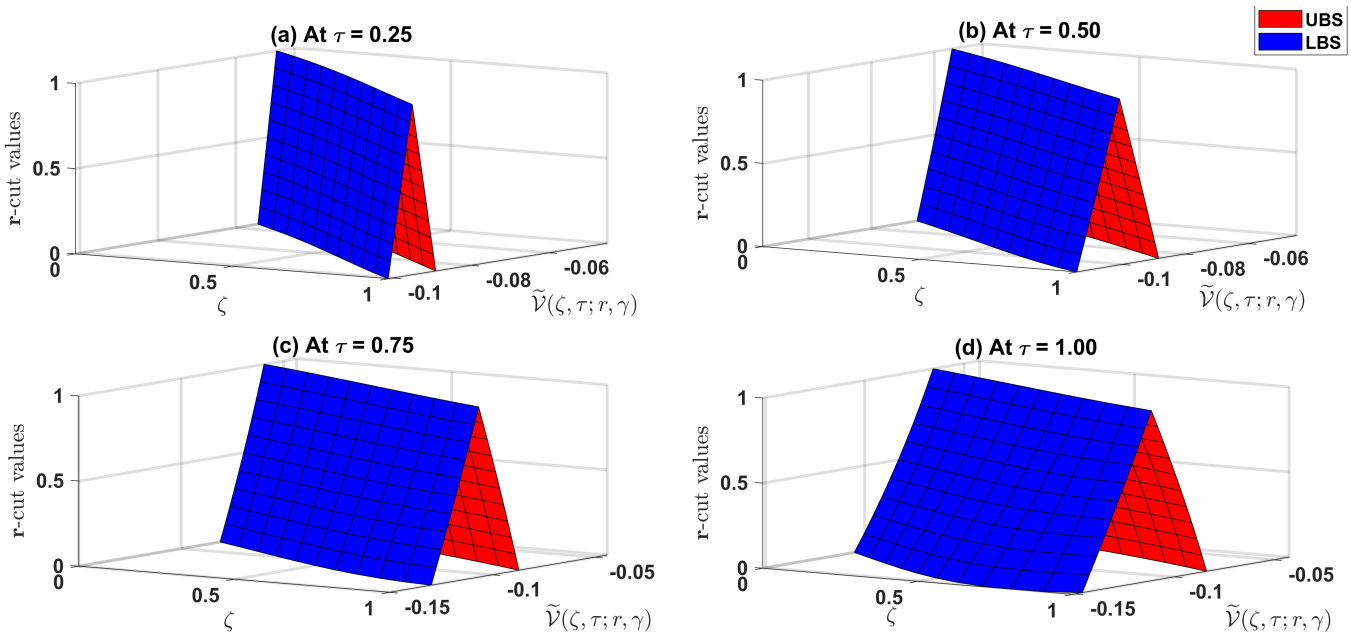

Figure 10: TFNs plots for $\widetilde{\mathcal{V}}$ at $q = -1, w = 9$ and different values of τ.

Fig. 9 and 10 showcase the behavior of TFNs for $\widetilde{\mathcal{U}}$ and $\widetilde{\mathcal{V}}$ under varying conditions. Both figures feature 3D plots that illustrate the relationship between the spatial variable ζ, the fuzzy variables $\widetilde{\mathcal{U}}$ and $\widetilde{\mathcal{V}}$, and their corresponding

r-cuts for different time values (τ). In Fig. 9, four subplots depict how $\widetilde{\mathcal{U}}$ evolves as τ progresses from 0.25 to 1.00. The blue surfaces represent the LBS, while the red surfaces indicate the UBS. Similarly, The figures presented in Fig. 10 demonstrate the changes in the shapes and positions of fuzzy numbers as τ increases, providing insight into how $\widetilde{\mathcal{U}}$ and $\widetilde{\mathcal{V}}$ depend on various parameters. The blue surfaces represent the LBS, while the red surfaces indicate the UBS. Such illustrations effectively enhance our understanding of the role of TFNs in managing uncertainty. It is worth noting that these findings highlight the importance of managing uncertainty in various settings.

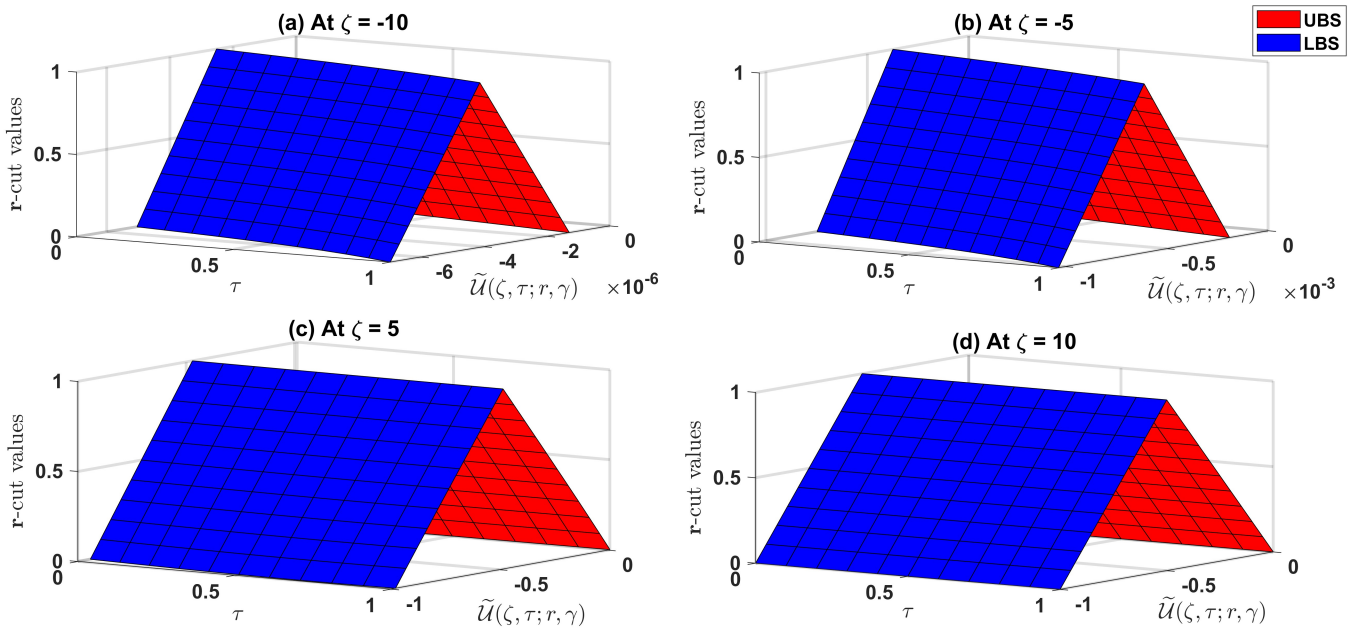

Figure 11: TFNs plots for $\widetilde{\mathcal{U}}$ at $q=-1, w=9$ and different values of ζ.

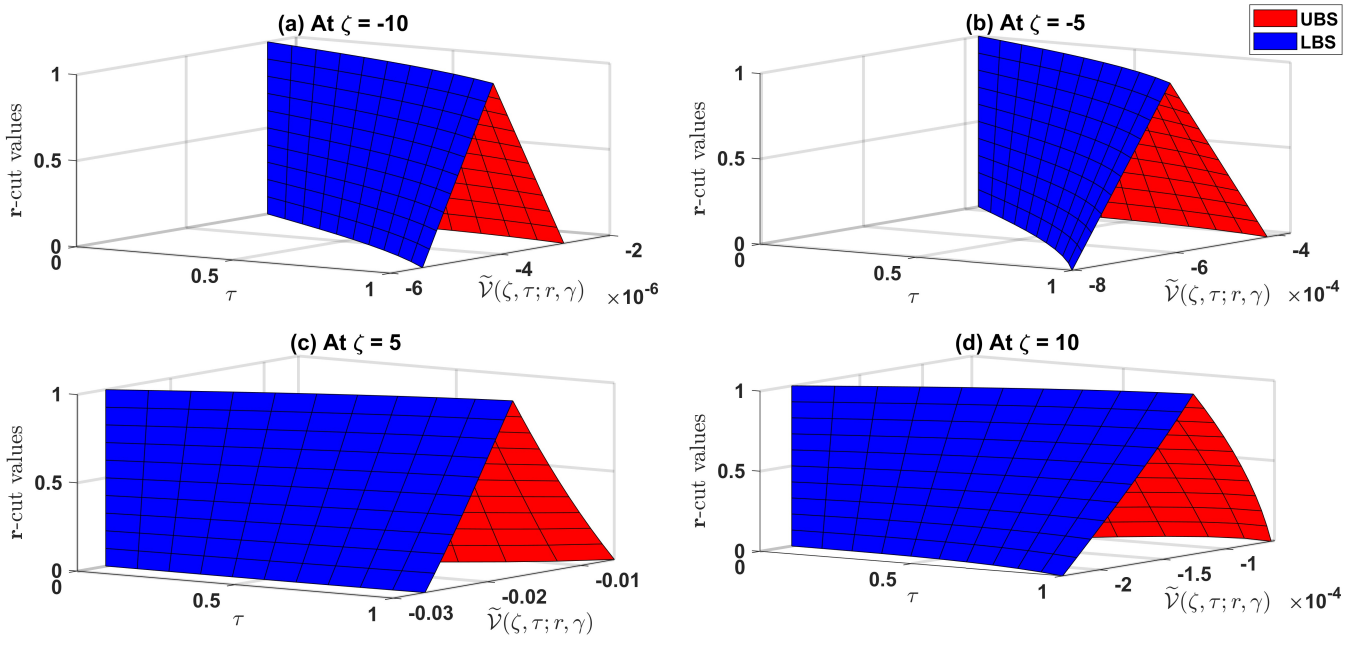

Figure 12: TFNs plots for $\widetilde{\mathcal{V}}$ at $q=-1, w=9$ and different values of ζ.

Fig. 11 and 12 depict the TFNs plots for $\widetilde{\mathcal{U}}(\zeta,\tau;r,\gamma)$ and $\widetilde{\mathcal{V}}(\zeta,\tau;r,\gamma)$, respectively, here ζ is varied while keeping $q=-1$ and $w=9$. The LBS and UBS are represented in blue and red, respectively, while r-cut values, indicating the degree of membership, are displayed along the z-axis. As ζ becomes more negative ($\zeta=-10$ and -5), the boundaries spread out wider, reflecting higher uncertainty. In context, for positive ζ values (such as $\zeta=5$ and 10), the boundaries are closer, indicating narrower ranges and reduced uncertainty. The x-axis displays the respective variables, while the y-axis represents τ. These visualizations highlight the dynamic behavior of TFNs, with both $\widetilde{\mathcal{U}}$ and $\widetilde{\mathcal{V}}$ exhibiting similar patterns, though differing in scale and position.

6 Conclusions

The study deals with the successful implementation of the FEADM to cBBEs in both crisp and fuzzy contexts. By proposing TFNs to model the vagueness instead in initial conditions, the method proves itself capable of solving problems when fluid dynamics parameter values are uncertain. Comparing the present results against HPM and OHAM, the further superiority of FEADM in terms of accuracy and efficiency is unveiled. The numerical study showed that the FEADM has smaller errors for the variables $\mathcal{U}$ and $\mathcal{V}$, proving it as a method specific enough for correct approximation of highly nonlinear systems. The theoretical convergence of the method gives credence to its convergence history and applicability. One very important observation is that the ranges have expanded, concerning the lower and upper bounds, as the parameters ζ and τ are increased. This pattern shows that fuzzy solutions change a lot when these values change, so we need strong methods like FEADM to handle and measure these uncertainties properly. The present study can be extended by implementing fuzzy extensions of numerical techniques such as the Crank–Nicolson and the Finite Element schemes. Additionally, exploring other fuzzy representations like trapezoidal and Gaussian fuzzy numbers may provide deeper insights into modeling uncertainties in nonlinear wave equations.

Acknowledgement

The authors wish to express their appreciation for several excellent suggestions for improvements in this paper made by the referees.

References

[1] H. Abdel-Gawad, M. Tantawy, *On controlled propagation of long waves in nonautonomous boussinesq-burgers equations*, Nonlinear Dynamics, **87** (2017), 2511-2518. https://doi.org/10.1007/s11071-016-3207-1

[2] Z. Ayati, J. Biazar, *On the convergence of homotopy perturbation method*, Journal of the Egyptian Mathematical Society, **23**(2) (2015), 424-428. https://doi.org/10.1016/j.joems.2014.06.015

[3] M. Benosman, J. Borggaard, O. San, B. Kramer, *Learning-based robust stabilization for reduced-order models of 2d and 3d boussinesq equations*, Applied Mathematical Modelling, **49** (2017), 162-181. https://doi.org/10.1016/j.apm.2017.04.032

[4] M. J. Dong, S. F. Tian, X. W. Yan, T. T. Zhang, *Nonlocal symmetries, conservation laws and interaction solutions for the classical boussinesq-burgers equation*, Nonlinear Dynamics, **95** (2019), 273-291. https://doi.org/10.1007/s11071-018-4563-9

[5] Z. Eidinejad, R. Saadati, C. Li, M. Inc, J. Vahidi, *The multiple exp-function method to obtain soliton solutions of the conformable date-jimbo-kashiwara-miwa equations*, International Journal of Modern Physics B, **38**(03) (2024), 2450043. https://doi.org/10.1142/S0217979224500437

[6] Z. Eidinejad, R. Saadati, J. Vahidi, C. Li, *Numerical solutions of 2d stochastic time-fractional sine-gordon equation in the caputo sense*, International Journal of Numerical Modelling: Electronic Networks, Devices and Fields, **36**(6) (2023), e3121. https://doi.org/10.1002/jnm.3121

[7] T. M. Elzaki, *The new integral transform Elzaki transform*, Global Journal of Pure and Applied Mathematics, **7**(1) (2011), 57-64. https://www.researchgate.net/publication/289123241

[8] T. M. Elzaki, *Application of new transform "Elzaki Transform" to partial differential equations*, Global Journal of Pure and Applied Mathematics, **7**(1) (2011), 65-70. https://www.researchgate.net/publication/236230758

[9] T. M. Elzaki, S. M. Elzaki, E. A. Elnour, *On the new integral transform "Elzaki Transform" fundamental properties investigations and applications*, Global Journal of Mathematical Sciences: Theory and Practical, **4**(1) (2012), 1-13. https://www.researchgate.net/publication/258316406

[10] X. Y. Gao, Y. J. Guo, W. R. Shan, *Beholding the shallow water waves near an ocean beach or in a lake via a boussinesq-burgers system*, Chaos, Solitons and Fractals, **147** (2021), 110875. https://doi.org/10.1016/j.chaos.2021.110875

[11] X. Y. Gao, Y. J. Guo, W. R. Shan, *On the oceanic/laky shallow-water dynamics through a boussinesq-burgers system*, Qualitative Theory of Dynamical Systems, **23**(2) (2024), 57. https://doi.org/10.1007/s12346-023-00905-w

[12] X. T. Gao, B. Tian, T. Y. Zhou, Y. Shen, C. H. Feng, *For the shallow water waves: Bilinear-form and similarity-reduction studies on a boussinesq-burgers system*, International Journal of Theoretical Physics, **63**(7) (2024), 179. https://doi.org/10.1007/s10773-024-05715-7

[13] P. Guo, X. Wu, L. Wang, *New multiple-soliton (kink) solutions for the high-order boussinesq-burgers equation*, Waves in Random and Complex Media, **26**(3) (2016), 383-396. https://doi.org/10.1080/17455030.2016.1158885

[14] A. Gupta, S. S. Ray, *Comparison between homotopy perturbation method and optimal homotopy asymptotic method for the soliton solutions of boussinesq-burger equations*, Computers and Fluids, **103** (2014), 34-41. https://doi.org/10.1016/j.compfluid.2014.07.008q

[15] O. E. Ige, R. A. Oderinu, T. M. Elzaki, *Adomian polynomial and elzaki transform method for solving klein gordon equations*, International Journal of Applied Mathematics, **32**(3) (2019), 451. https://www.researchgate.net/publication/335276371

[16] Y. L. Jiang, C. Chen, *Lie group analysis and dynamical behavior for classical boussinesq-burgers system*, Nonlinear Analysis: Real World Applications, **47** (2019), 385-397. https://doi.org/10.1016/j.nonrwa.2018.11.010

[17] P. Karunakar, S. Chakraverty, *Effect of coriolis constant on geophysical korteweg-de vries equation*, Journal of Ocean Engineering and Science, **4**(2) (2019), 113-121. https://doi.org/10.1016/j.joes.2019.02.002

[18] P. Karunakar, S. Chakraverty, *Homotopy perturbation method for predicting tsunami wave propagation with crisp and uncertain parameters*, International Journal of Numerical Methods for Heat and Fluid Flow, **31**(1) (2020), 92-105. https://doi.org/10.1108/HFF-11-2019-0861

[19] P. Karunakar, S. Chakraverty, T. Rao, K. Ramesh, A. Hussein, *Fuzzy fractional shallow water wave equations: Analysis, convergence of solutions, and comparative study with depth as triangular fuzzy number*, Physica Scripta, **99**(12) (2024), 125216. https://doi.org/10.1088/1402-4896/ad8afd

[20] M. Khalfallah, *Exact traveling wave solutions of the boussinesq-burgers equation*, Mathematical and Computer Modelling, **49**(3-4) (2009), 666-671. https://doi.org/10.1016/j.mcm.2008.08.004

[21] R. Kumar, K. S. Pandey, A. Kumar, *Dynamical behavior of the solutions of coupled boussinesq-burgers equations occurring at the seaside beaches*, Brazilian Journal of Physics, **52**(6) (2022), 201. https://doi.org/10.1007/s13538-022-01195-4

[22] S. Kumar, S. Rani, *Symmetries of optimal system, various closed-form solutions, and propagation of different wave profiles for the boussinesq-burgers system in ocean waves*, Physics of Fluids, **34**(3) (2022). https://doi.org/10.1063/5.0085927

[23] X. Li, A. Chen, *Darboux transformation and multi-soliton solutions of boussinesq-burgers equation*, Physics Letters A, **342**(5-6) (2005), 413-420. https://doi.org/10.1016/j.physleta.2005.05.083

[24] M. Li, W. Hu, C. Wu, *Rational solutions of the classical boussinesq-burgers system*, Nonlinear Dynamics, **94** (2018), 1291-1302. https://doi.org/10.1007/s11071-018-4424-6

[25] Z. Liang, Z. L. Feng, L. C. Yin, *Some new exact solutions of Jacobian elliptic function about the generalized boussinesq equation and boussinesq-burgers equation*, Chinese Physics B, **17**(2) (2008), 403. https://doi.org/10.1088/1674-1056/17/2/009

[26] F. Y. Liu, Y. T. Gao, *Lie group analysis for a higher-order boussinesq-burgers system*, Applied Mathematics Letters, **132** (2022), 108094. https://doi.org/10.1016/j.aml.2022.108094

[27] M. Liu, H. Xu, Z. Wang, *Exact solutions and bifurcations of the time-fractional coupled boussinesq-burgers equation*, Physica Scripta, **98**(11) (2023), 115040. https://doi.org/10.1088/1402-4896/ad03c4

[28] J. Lu, Y. Sun, *Numerical approaches to time fractional boussinesq-burgers equations*, Fractals, **29**(08) (2021), 2150244. https://doi.org/10.1142/S0218348X21502443

[29] B. A. Mahmood, M. A. Yousif, *A residual power series technique for solving boussinesq-burgers equations*, Cogent Mathematics, **4**(1) (2017), 1279398. https://doi.org/10.1080/23311835.2017.1279398

[30] A. M. Mubaraki, R. Nuruddeen, K. K. Ali, J. Gómez-Aguilar, *Additional solitonic and other analytical solutions for the higher-order boussinesq-burgers equation*, Optical and Quantum Electronics, **56**(2) (2024), 165. https://doi.org/10.1007/s11082-023-05744-2

[31] Z. M. Odibat, *A study on the convergence of homotopy analysis method*, Applied Mathematics and Computation, **217**(2) (2010), 782-789. https://doi.org/10.1016/j.amc.2010.06.017

[32] A. Podder, M. A. Arefin, K. A. Gepreel, M. H. Uddin, M. A. Akbar, *Diverse soliton wave profile assessment to the fractional order nonlinear landau-ginzburg-higgs and coupled boussinesq-burger equations*, Results in Physics, **65** (2024), 107994. https://doi.org/10.1016/j.rinp.2024.107994

[33] A. A. Rady, M. Khalfallah, *On soliton solutions for boussinesq-burgers equations*, Communications in Nonlinear Science and Numerical Simulation, **15**(4) (2010), 886-894. https://doi.org/10.1016/j.cnsns.2009.05.039

[34] A. A. Rady, E. Osman, M. Khalfallah, *Multi-soliton solution, rational solution of the boussinesq-burgers equations*, Communications in Nonlinear Science and Numerical Simulation, **15**(5) (2010), 1172-1176. https://doi.org/10.1016/j.cnsns.2009.05.053

[35] P. Rao, D. Mohapatra, S. Chakraverty, D. Roy, *Vibration analysis of non-homogenous single-link flexible manipulator in uncertain environment*, Applied Mathematical Modelling, (2025), 115939. https://doi.org/10.1016/j.apm.2025.115939

[36] X. Rui, *Darboux transformations and soliton solutions for classical boussinesq-burgers equation*, Communications in Theoretical Physics, **50**(3) (2008), 579. https://doi.org/10.1088/0253-6102/50/3/08

[37] M. Sahoo, S. Chakraverty, *Dynamics of tsunami wave propagation in uncertain environment*, Computational and Applied Mathematics, **43**(5) (2024), 266. https://doi.org/10.1007/s40314-024-02776-6

[38] D. Shi, Y. Zhang, W. Liu, J. Liu, *Some exact solutions and conservation laws of the coupled time-fractional boussinesq-burgers system*, Symmetry, **11**(1) (2019), 77. https://doi.org/10.3390/sym11010077

[39] R. Vana, P. Karunakar, *A fuzzy semi-analytical approach for modeling uncertainties in solitary wave solution of coupled nonlinear boussinesq equations*, Physica Scripta, **99**(10) (2024), 105218. https://doi.org/10.1088/1402-4896/ad72aa

[40] R. Vana, P. Karunakar, *Computational approach and convergence analysis for intervalbased solution of the benjamin-bona-mahony equation with imprecise parameters*, Engineering Computations: International Journal for Computer-Aided Engineering, **41**(4) (2024), 1067-1085. https://doi.org/10.1108/EC-12-2023-0905

[41] R. Vana, P. Karunakar, *Fuzzy uncertainty modeling of generalized hirota-satsuma coupled korteweg-de vries equation*, Physics of Fluids, **36**(9) (2024), 096609. https://doi.org/10.1063/5.0226445

[42] R. Vana, P. Karunakar, *Uncertainties in regularized long-wave equation and its modified form: A triangular fuzzy-based approach*, Physics of Fluids, **36**(4) (2024), 046610. https://doi.org/10.1063/5.0206452

[43] R. Vana, K. Perumandla, S. Chakraverty, *Semi-analytical and numerical computations for the solution of uncertain fractional benjamin bona mahony equation with triangular fuzzy number*, Journal of Computational Applied Mechanics, **56**(1) (2025), 196-221. https://doi.org/10.22059/jcamech.2024.387317.1318

[44] A. C. Varsoliwala, T. R. Singh, *An approximate analytical solution of non linear partial differential equation for water infiltration in unsaturated soils by combined elzaki transform and adomian decomposition method*, in: Journal of Physics: Conference Series, Vol. 1473, IOP Publishing, (2020), 012009. https://doi.org/10.1088/1742-6596/1473/1/012009

[45] A. C. Varsoliwala, T. R. Singh, *Mathematical modeling of tsunami wave propagation at mid ocean and its amplification and run-up on shore*, Journal of Ocean Engineering and Science, **6**(4) (2021), 367-375. https://doi.org/10.1016/j.joes.2021.03.003

[46] A. C. Varsoliwala, T. R. Singh, *Solution of fingering phenomenon arising in porous media in horizontal direction by combination of elzaki transform and adomian decomposition method*, in: Advances in Mathematical Modelling, Applied Analysis and Computation: Proceedings of ICMMAAC 2021, Springer, (2022), 495-506. https://doi.org/10.1007/978-981-19-0179-9_29

[47] A. C. Varsoliwala, T. R. Singh, *Mathematical modeling of atmospheric internal waves phenomenon and its solution by elzaki adomian decomposition method*, Journal of Ocean Engineering and Science, **7**(3) (2022), 203-212. https://doi.org/10.1016/j.joes.2021.07.010

[48] Y. H. Wang, *CTE method to the interaction solutions of boussinesq-burgers equations*, Applied Mathematics Letters, **38** (2014), 100-105. https://doi.org/10.1016/j.aml.2014.07.014

[49] K. J. Wang, G. D. Wang, H. W. Zhu, *A new perspective on the study of the fractal coupled boussinesq-burger equation in shallow water*, Fractals, **29**(05) (2021), 2150122. https://doi.org/10.1142/S0218348X2150122X

[50] C. C. Zhang, A. H. Chen, *Bilinear form and new multi-soliton solutions of the classical boussinesq-burgers system*, Applied Mathematics Letters, **58** (2016), 133-139. https://doi.org/10.1016/j.aml.2016.02.015

[51] Y. Zhang, L. Wang, *Application of laplace adomian decomposition method for fractional fokker-planck equation and time fractional coupled boussinesq-burger equations*, Engineering Computations, **41**(4) (2024), 793-818. https://doi.org/10.1108/EC-06-2023-0275

[52] P. M. Zu, X. M. Zhang, *Study of the generalized hypothetical syllogism for some well known families of fuzzy implications with respect to strict t-norm*, Iranian Journal of Fuzzy Systems, **21**(2) (2024), 181-200. https://doi.org/10.22111/ijfs.2024.46361.8164

[53] J. M. Zuo, Y. M. Zhang, *The hirota bilinear method for the coupled burgers equation and the high-order boussinesq-burgers equation*, Chinese Physics B, **20**(1) (2011), 010205. https://doi.org/10.1088/1674-1056/20/1/010205